https://doi.org/10.1016/j.ijmecsci.2022.107552

Hybrid electromagnetic shunt damper with Coulomb friction and negative impedance converter

Ruqi Sun, Waion Wong*, Li Cheng
Department of Mechanical Engineering
The Hong Kong Polytechnic University, Hong Kong, PRC

Abstract:

Electromagnetic shunt damper (EMSD) offers flexible tunability of linear damping. The low damping force-to-mass ratio of the EMSD, however, hinders those applications which require large damping force. Adding a negative impedance shunt in EMSD circuit can increase its damping force and broaden its effective frequency range at the expense of causing possible instabilities in the control circuit. On the other hand, Coulomb friction damper (FD) can offer a higher damping force-to-mass ratio than EMSD but it is difficult to be precisely controlled due to its nonlinear characteristics and excessive frequency sensitivity. This paper examines, both theoretically and experimentally, two types of hybrid dampers: one combining an EMSD and a Coulomb friction damper (EMSD+FD), and the other EMSD with a voltage negative impedance converter (EMSD+VNIC). Through proper control of the additional damping arising from FD and VNIC, the problem of unstable ESMD+VNIC and the excessive frequency sensitivity of the FD are alleviated. A prototype of EMSD+VNIC+FD is built and tested. The damping force provided by the FD in the prototype is varied by adjusting the normal force applied by a compression spring, while that from the EMSD+VNIC is controlled by adjusting the shunt circuit impedance with a variable resistor. The maximized tunability of the two enhancement methods provides a ninefold increase of the tunable damping range and a sixfold increase of the damping force-to-mass ratio of the EMSD. The proposed EMSD+VNIC+FD is finally applied and tested experimentally to achieve H_∞ optimization of a ground-hooked dynamic vibration absorber for the minimization of resonant vibration of a single-degree-of-freedom system.

Keywords:

Electromagnetic shunt damper, Enhancement methods, Hybrid damper, Coulomb friction, Negative impedance

* Corresponding author.
E-mail address: mmwowong@polyu.edu.hk (Waion Wong)

Nomenclature:

DVA	Dynamic vibration absorber	EMF	Electromotive force
EMSD	Electromagnetic shunt damper	FD	Friction damper
MDOF	Multi-degree-of-freedom	OP-AMP	Operational amplifier
PWM	Pulse width modulation	SDOF	Single-degree-of-freedom
VNIC	Voltage negative impedance converter		

1. Introduction

Able to achieve mechanical to electrical energy conversion, electromagnetic shunt dampers (EMSDs) have been widely used for energy harvesting [1,2], dual-functional energy harvesting and vibration control [3-7], and self-sensing [8,9] since the EMSD concept was firstly proposed by Behrens et al. [10]. Despite the enormous potential it offers, EMSD has not been widely used for vibration control because of its low damping force-to-mass ratio as compared with other types of vibration dampers. Open literature also shows an insufficient effort in exploring feasible ways to achieve enhanced vibration control performance using EMSDs. In this introduction part, existing works on EMSD circuits and structure design are reviewed firstly, covering both linear and nonlinear systems. Then more specific development on hybrid dampers by combining EMSD and friction damper (FD) is highlighted, demonstrating the existing factors that hinder FD applications. Finally, ground-hooked DVAs, which require larger damping than the traditional DVAs, are briefly discussed from the damping calibration perspective.

Passive EMSD for linear vibration control heavily relies on the shunt impedance and the transduction factor for the tunable range enhancement. Since the damping coefficient is inversely proportional to the shunt impedance, negative impedance was added to compensate for the coil internal resistance in order to improve the tunable range. In this regard, Yan et al. [11] first introduced the negative impedance shunts to enhance the damping range and broaden the effective frequency range of EMSD. Stabile et al. [12], Li and Zhu [13] proposed a simplified voltage negative impedance converter (VNIC) with a high-power operational amplifier (OP-AMP). Zhou et al. [14] adopted negative impedance for damping improvement of EMSD using various optimization strategies. Negative resistance was also applied on a cylindrical cam EMSD which allows for the motion mode conversion from translation to rotation [15]. Berardengo et al. [16] and many other researchers have done similar works by adding negative impedance shunts to enhance piezoelectric shunt damping. One common and key issue pertinent to VNIC is the possible occurrence of instability when the total circuit impedance in an EMSD is near zero.

Alongside the effort in exploring negative impedance shunts, various methods have also been applied to achieve an optimal shunt to cope with specific vibration control objectives. Behrens et al. [17] first calculated the optimal damping resistance of an EMSD for resonant vibration mitigation. Zhou et al. [14] investigated the optimum

resistive-inductive-capacitive shunt circuit of EMSD with negative impedance. Four types of shunt circuits were compared by Li and Zhu [18] to cope with various frequency spectra when used for linear vibration isolation. Pulse width modulation (PWM) was used in a chopper by Auleley et al. [19] and an H-bridge circuit by Li and Zhu [20] to obtain digital tuning shunts. Besides the pre-designed optimal shunts, different controllers can also be employed to tune the shunt impedance in order to cope with changing conditions. Relevant works include Niederberger et al. [21] which proposed a resistor-capacitor controller to improve the robustness of an EMSD under various operating conditions. McDaid and Mace [22] used a model-based feedforward controller to tune the effective mechanical stiffness and damping of an EMSD. With the aid of a microcontroller, a self-powered EMSD can easily switch between a passive energy harvesting mode and a semi-active control mode [23]. Similar self-powered EMSD with active control was also proposed by Li and Zhu [20]. Paknejad et al. [24] proposed a hybrid EMSD with active control and velocity feedback which consume less power than a pure active control system, and has a higher tolerance than a pure passive control system. More details about shunt damping vibration control technology can be found in the review paper by Yan et al. [25].

The other crucial parameter governing the tunable range is the transduction factor, which relates the electromotive force (EMF) to the relative velocity between the moving mass and the coil of the EMSD. Depending on the structural EMSD parameters, the transduction factor has received much less attention than the shunt. Among existing efforts, Kremer and Liu [26] proposed an EMSD model with a single magnet and coil for transduction factor estimation. Sun et al. [27] investigated the linear EMSD enhancement with opposing magnets configuration, and compared it with similar EMSD designs of Stabile et al. [12] and Zuo et al. [28]. Sun et al. [29] also established the optimal number of opposing magnet pairs in series in the EMSD to ensure the maximum damping force. Some other auxiliary mechanisms could also lead to increased transduction in the EMSD including the level-type EMSD [30] and gearbox-added rotary EMSD [31].

EMSD was also used for nonlinear vibration control. Ma et al. [32] proposed the design of a nonlinear EMSD by adjusting structural parameters including the spacer height and coil positions. Yan et al. [33] proposed a stiffness-varying nonlinear isolator with magnetic effects. Yan et al. [34] also proposed a bistable isolator using a special positioning configuration of EMSD magnets. Both isolators showed good performance for nonlinear vibration isolation. Apart from structural parameter adjustment, Auleley et al. [19] showed that the natural frequency of electromagnetic shunt could also be varied by introducing a digital pulse width modulator to the EMSD.

With careful design of shunt circuits and structural parameters, EMSDs have been widely applied in various ways to cope with very diversified applications, including micro-vibration mitigation on space crafts [12], locker at bridge cables [35,36], energy harvesting on railroad transportation [37], dual-function of energy harvesting and vibration control on automotive suspensions [2, 38], semi-active control on seat suspensions [39], frame structures vibration control [40], and energy capturing from

human motion [41,42], etc.

Besides the exploration on EMSDs themselves, hybrid dampers with other types of dampers have been proposed recently. A tunable hybrid damper combining Coulomb friction and electromagnetic shunt damping has been shown to significantly improve the tunable damping range of an EMSD [43]. The proposed hybrid damper was applied to a dynamic vibration absorber (DVA) to provide the optimal damping force for the minimization of the resonant vibration of a single-degree-of-freedom (SDOF) primary structure. Nonlinearity and stick-slip behaviors of the FD are the major issues to be tackled. Den Hartog [44] theoretically investigated the forced vibration problem of a SDOF system with Coulomb friction damping under harmonic excitation decades ago and derived the steady-state solution. Menq et al. [45] investigated the forced vibration problem with variable normal load of FD. Lee et al. [46] then designed a tunable FD based on the results of Menq et al. With the evaluation of vibration transmissibility and energy flow, Dai et al. [47] showed that FD can be designed specifically for the purpose of energy dissipation or transmission.

Stick-slip phenomena may occur to increase the motion uncertainty when the excitation force is not high enough to overcome the static friction in a FD. The corresponding stick-slip boundaries of the FD, when applied to single-degree-of-freedom (SDOF) and multi-degree-of-freedom (MDOF) systems, have been analytically investigated by Marino et al. [48,49] in detail. Scholl et al. [50] evaluated the stick-slip effects by comparing the experimental and numerical results. Micro-slip induced dry friction damping of a frictional joint interface was investigated by Chen and Deng [51] to show the stick-slip regions with loads. Zhou et al. [52] adopted the LuGre model to capture the stick-slip state of a gas foil bearing system. Results showed that the LuGre model performs better than the smooth friction model [53] with moderate and high smoothing parameters. Available modeling methods of FD have been reviewed by Ferri [54] and Gagnon et al. [55].

To overcome the uncertainties relating to FD, observer and feedback devices are required to monitor and compensate for the nonlinear friction of the damper. Ruderman and Iwasaki [56] developed an observer of nonlinear friction dynamics for system identification with a linear feedback loop. More works about friction compensation are reviewed by Huang et al. [57]. Due to the complexity of the FD, only a few real applications on vibration damping can be found, exemplified by bridge cables vibration [58], and DVA optimization [59].

As an effective vibration suppression device, the traditional DVA mentioned above has been investigated by Den Hartog [60], and this technique can mitigate the resonant vibration of a SDOF primary system significantly with optimal damping. A variant ground-hooked DVA was proposed by Ren [61] with better vibration absorption performance. Comparisons between ground-hooked and traditional DVAs with EMSD were conducted, both analytically [62] and experimentally [3]. Moreover, Cheung and Wong [63] showed an improved design of the aforementioned ground-hooked DVA than the one derived by Ren [61]. However, the optimal design of the ground-hooked

DVA proposed by Cheung and Wong [63] requires a much higher damping ratio than the one by Ren. Maintaining a high damping force-to-mass ratio, the proposed hybrid damper proposed was applied to a ground-hooked DVA to provide experimental validation of the optimal design of the ground-hooked DVA predicted by Cheung and Wong [63].

Theoretically, the similarities between DVA and EMSD have been investigated and classified [64]. With only resistance in the shunt circuit, the linear EMSD can be regarded as a pure damper without affecting the stiffness in the system. When the shunt contains suitable resistance and capacitance, the EMSD can be coupled to a DVA to improve its damping performance [65]. The analytical and numerical H_∞ and H_2 optimizations of EMSD were derived to suppress single-mode vibration [66] and multi-mode vibration [67] when the EMSD works as a resonant absorber.

EMSD is not widely used in large machinery and structures because of its low damping force-to-mass or size ratio. The transduction factor of the EMSD coil can be enhanced by increasing the radius or turns of the coil and the size of magnets inside the coil; but the weight and the size of the EMSD will also be increased. The damping force and the tunable damping range of EMSDs can be significantly improved by adding a VNIC to the EMSD circuit, but the induced large current, when the shunt circuit impedance is near zero, can cause increased heat generation in the circuit, which is not desirable. Additional accessories for cooling would make the system bulky. Therefore, EMSD with VNIC also has its limitations for real-life applications. On the other hand, Coulomb friction damper can offer a much higher damping force-to-mass or size ratio than EMSD despite its obvious difficulty in being precisely controlled due to its nonlinear characteristics and its excessive frequency sensitivity.

Based on the above-mentioned reasons, this paper proposes the simultaneous use of FD and VNIC to improve the tunable range of an EMSD through acquiring precise and variable damping tuning for vibration control applications. It is shown that the two enhancement methods can supplement each other with their respective constraints avoided, if they are properly designed and implemented into an EMSD with the procedure to be established in this paper. Examples demonstrate a roughly 900% increase in the tunable range of the damping coefficient using the proposed enhancement method. To show its efficacy for vibration control which requires a precise and high level of damping, the enhanced EMSD is prototyped and experimentally tested to achieve the optimized H_∞ control in a ground-hooked DVA. To the best knowledge of the authors, this is the first report on the experimental verification of H_∞ optimization of a ground-hooked DVA proposed theoretically by Cheung and Wong [63]. The main contribution of this paper is two-fold: 1) achievement of a significant enhancement of the EMSD tunable range with the aid of FD and VNIC; 2) avoidance of unstable EMSD with VNIC and excessive frequency sensitivity of the FD with a proper balance between the two enhancement methods.

The rest of the paper is organized as follows. Section 2 introduces and compares the damping characteristics of the proposed hybrid EMSD with FD or VNIC. Section 3

describes the structural parameters of the proposed hybrid damper and verifies the damping coefficient enhancement with experimental tests. Section 4 presents the application of both enhancement methods to achieve H_∞ optimization in the design of ground-hooked DVA and analyses the appropriate combination of each. Section 5 summarizes the results and main conclusions.

2. Theoretical analyses of the proposed hybrid dampers and DVA

In this section, the theoretical models of the proposed hybrid dampers, namely EMSD with FD and EMSD with VNIC, are established. The tunable damping features of each hybrid damper are elaborated for the onsite tuning strategy development. The damping force spectra of the FD are analyzed to gain a better understanding of the nonlinear characteristics of the FD. Both enhancement methods are combined and applied for the damping enhancement of the EMSD. Moreover, the proposed hybrid EMSD based damper with FD and VNIC is applied to a ground-hooked DVA to achieve H_∞ optimization. Theoretical prediction of the system response using the optimized DVA is presented and discussed.

2.1 Enhancement methods

The proposed damping enhancement methods for an EMSD are investigated, including adding a FD in parallel with the EMSD and generating negative impedance in the shunt circuit by using a VNIC. The working principles of each enhancement method and tunable parameters are enlightened and discussed in the following sections.

2.1.1 EMSD+FD

A tunable hybrid damper is shown in Fig. 1a with FD and EMSD connected in parallel. The damping force can be tuned by adjusting the normal force F_N of the FD and the external resistance R_{load} of the EMSD. The damping coefficient of linear EMSD can be calculated based on the electromechanical coupling analysis. As for FD, the equivalent damping coefficient can be derived by equating the energy dissipation per cycle of the FD and linear viscous damping. The hybrid damping coefficient, c, can be expressed as

$$c = c_e + c_f = \frac{K_t^2}{Z} + \frac{4\mu_f F_N}{\pi\omega X} \tag{1}$$

where c_e denotes the damping coefficient of the EMSD; c_f the equivalent damping coefficient of FD; K_t the transduction factor of EMSD; Z the circuit impedance of the EMSD; μ_f the friction coefficient of the FD; F_N the normal force of the FD; ω the exciting frequency and X the vibration amplitude.

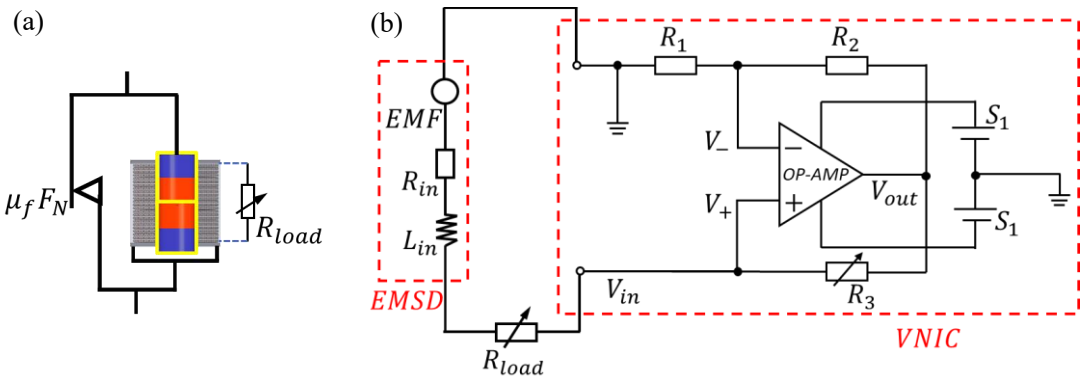

Fig. 1 Schematics of the proposed EMSD hybrid damper with (a) Coulomb friction damping force $\mu_f F_N$, (b) VNIC circuit. The friction damping force $\mu_f F_N$ can be adjusted by changing the normal force; the electromagnetic shunt damping can be tuned with the external resistance R_{load}. The key component in the VNIC is an OP-AMP, which is responsible for voltage amplification. The VNIC resistance can be adjusted by changing the resistance R_3.

2.1.2 EMSD+VNIC

The simplified VNIC in Fig. 1b is adopted for internal resistance compensation in the EMSD. Compared to the ESMD shunt in Fig. 1a, VNIC is connected with the external resistor in series. As the main functional component in the VNIC, an OP-AMP is responsible for the voltage amplification from V_{in} to V_{out}. With the assumption of $V_+ = V_-$, the equivalent resistance of the VNIC writes

$$R_{VNIC} = \frac{V_{in}}{i} = -\frac{R_1 R_3}{R_2} \tag{2}$$

where R_3 is a tunable resistance, R_1 and R_2 are constant resistance. The detailed derivation of equivalent resistance of VNIC is shown in Appendix A. With the compensation of VNIC, the total circuit impedance of the EMSD can be reduced to near zero.

$$Z = Z_{in} + R_{load} + R_{VNIC} \tag{3}$$

with Z_{in} denoting the internal impedance of the EMSD.

2.2 Combination

The two damping enhancement methods discussed above are proposed to be used together in EMSD design. The purpose of combining the two types of hybrid dampers is to solve the problems arising from each individual hybrid damper as discussed in the Introduction. Characteristics of the hybrid damping coefficient and damping force of each are analyzed and the optimum combination of the enhancement methods is proposed based on the analysis in this section.

2.2.1 Tuning device selection

Both aforementioned enhancement methods are expected to significantly improve the tunable damping range of the EMSD when applied separately. As illustrated in Fig. 2, enhancement methods are classified into three categories: *A* (EMSD + VNIC), *B* (EMSD + FD), *C* (EMSD +VNIC + FD). Regions in blue in both figures denote the damping provided by the tunable EMSD alone. Regions in red and gray correspond to the tunable EMSD + VNIC and tunable FD, respectively.

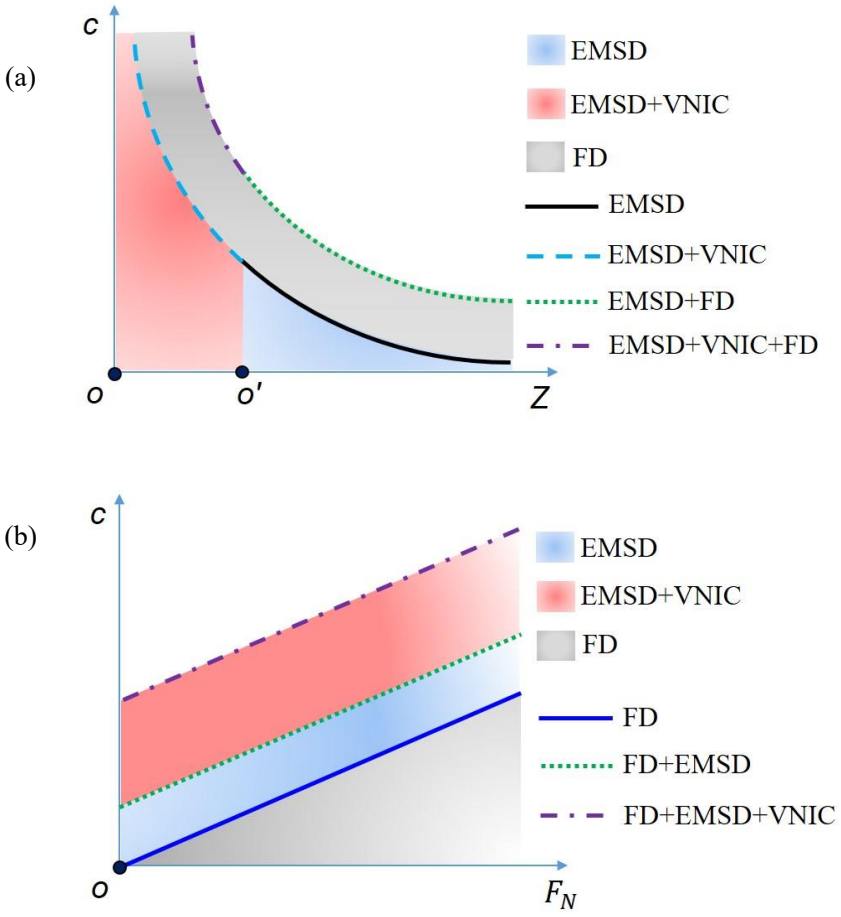

Fig. 2 Variations of the damping coefficient with different enhancement methods. (a) EMSD or (b) FD is selected as the tuning device. Regions in blue: tunable EMSD, red: tunable EMSD + VNIC, and gray: tunable FD.

EMSD damping tunable range with VNIC can be improved to the approachable level of the hybrid damper, in which case either an alteration in the FD or EMSD with VNIC can be regarded as the basic tuning strategy. The corresponding damping coefficient variation is shown in Fig. 2. With EMSD selected as the basic tuning strategy, the damping coefficient is inversely proportional to the shunt impedance as shown in Fig. 2a. The damping coefficient of the EMSD with VNIC increases rapidly when the shunt circuit impedance varies from O' $(Z = Z_{in})$ to O $(Z = 0)$. However, the required tuning precision of the resistance is much higher in this region. When FD is

used for damping tuning in Fig. 2b, the damping coefficient varies linearly with the normal force. The variation of the damping coefficient with both EMSD+FD and VNIC is less sensitive than that with EMSD as the damping tuning device. Fig. 2a and Fig. 2b show that VNIC contributes much to the damping improvement, but VNIC is not suitable for fine-tuning when the total circuit impedance approaches zero.

2.2.2 Hybrid damping force

When FD and VNIC are both deployed for EMSD enhancement, the resultant hybrid damping force needs to be quantified. Assuming $X\cos wt$ to be the relative displacement between the moving mass and the coil of the EMSD, the damping force of the EMSD with VNIC can be expressed as

$$F_e(t) = c_e wX \sin wt \tag{4}$$

The Coulomb friction of the FD is assumed to be a square wave with an amplitude $\mu_f F_N$, whose Fourier series decomposition can be written as

$$F_f(t) = \frac{4}{\pi}\mu_f F_N \left(\sin wt + \frac{1}{3}\sin 3wt + \frac{1}{5}\sin 5wt + \cdots \frac{1}{n}\sin nwt + \cdots\right) \tag{5}$$

where n is a positive odd number.

To compare the two types of damping, the damping force ratio of EMSD to FD, α, is defined as:

$$\alpha = \frac{max|F_e|}{max|F_f|} \tag{6}$$

With α = 5, both types of damping forces are plotted in Fig. 3 with ω = 1 and X = 1. As shown in Fig. 3a, the hybrid damping force still functions like a sinusoidal signal because of the high damping force ratio in this case. However, the frequency spectrum of the hybrid damping force (Fig. 3b) shows odd-order harmonics due to the FD, which are supposed to be impaired with increasing damping force ratio, to be investigated in Section 3.3.

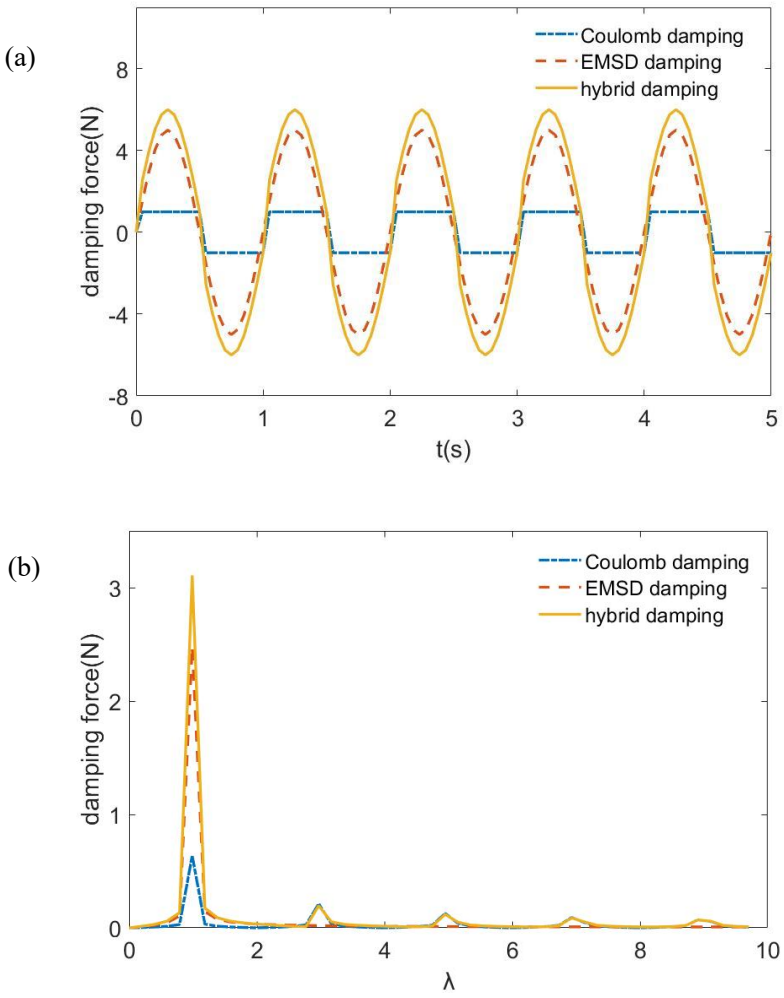

Fig. 3 Damping force of different dampers in (a) time domain and (b) frequency domain. The damping force ratio of the EMSD to FD is selected as $\alpha = 5$.

2.3 Ground-hooked DVA

To verify the achieved enhancement and the tunability of both EMSD + FD and EMSD + VNIC methods, both hybrid dampers are applied to a ground hooked DVA which requires a higher optimal damping ratio than the traditional DVA. As shown in Fig. 4a, one end of the enhanced EMSD is ground-hooked, while the other one is connected to the DVA mass m_2. In Fig. 4a, $F_0 \cos \omega t$ is a sinusoidal excitation. k_1, m_1, x_1 denote the stiffness, mass, and displacement of primary system, respectively. k_2, m_2, x_2 denote the stiffness, mass, and displacement of the DVA. c_f and c_e are the damping coefficient of the FD and the EMSD, respectively.

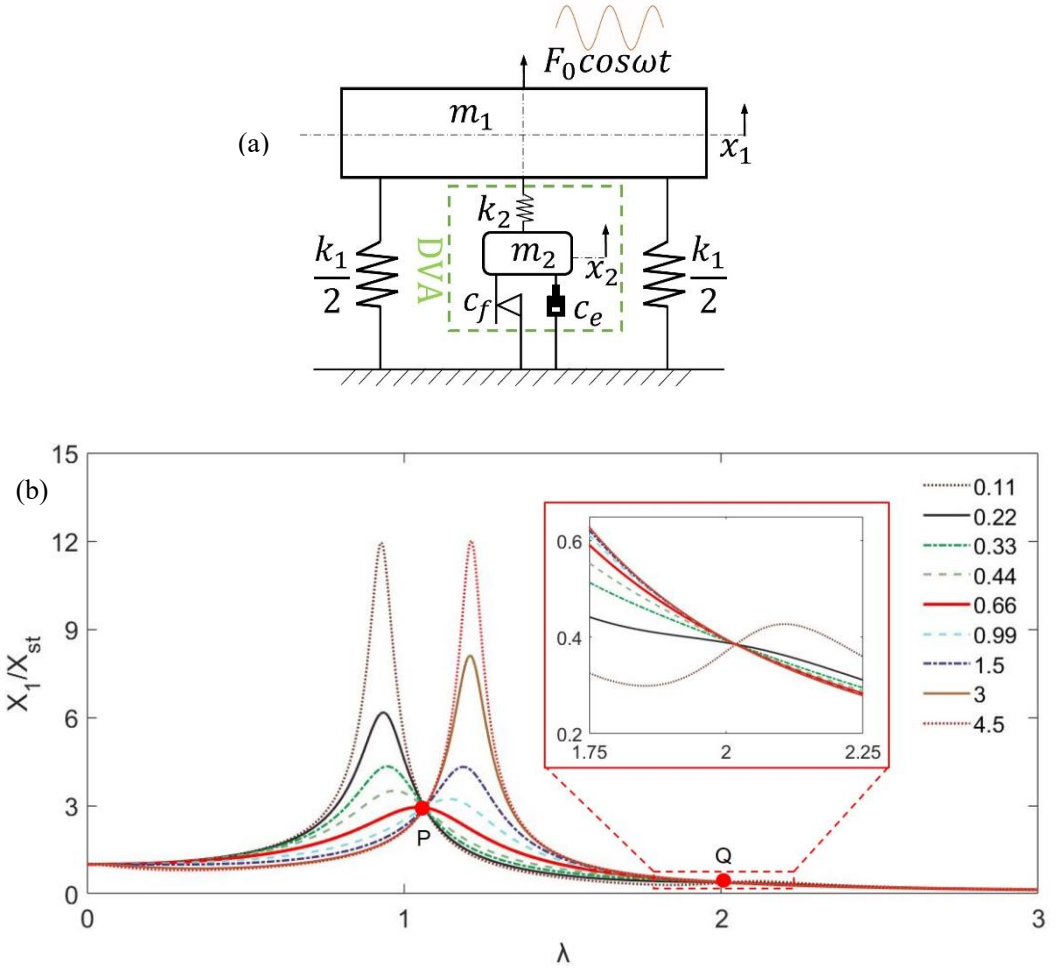

Fig. 4 (a) Schematic of a ground-hooked DVA with the enhanced EMSD under harmonic force excitation. (b) Displacement response X_1/X_{st} of m_1 with various damping ratios ξ when the ground-hooked DVA is optimized with the minimum resonant response at fixed point *P*. μ=0.1.

According to Cheung and Wong [63], the approximated optimal natural frequency ratio of the ground-hooked DVA can be obtained as

$$\gamma_{opti} = \begin{cases} 2.02 - 1.5\mu & 0.092 < \mu < 0.22 \\ \leq \sqrt{1/\mu} & 0.22 < \mu < 0.25 \end{cases} \tag{7}$$

where μ is the mass ratio between m_2 and m_1. The corresponding optimal damping can be derived and written as [63],

$$\xi_{opti} = \sqrt{\frac{1 - 2\gamma^2(1-\mu) + \gamma^4(1+\mu+\mu^2) - \left(1 - \gamma^2(1-\mu)\right)\sqrt{1 - 2(1-\mu)\gamma^2 + (1+\mu^2)\gamma^4}}{4\gamma^2\left(1 + \gamma^2 + \mu\gamma^2 - \sqrt{1 - 2(1-\mu)\gamma^2 + (1+\mu^2)\gamma^4}\right)}} \tag{8}$$

The dimensionless primary system response X_1/X_{st} is then depicted in Fig. 4b with a mass ratio $\mu = 0.1$ based on the equations of motion in Appendix B. The fixed-points *P* and *Q* are the keys to calibrate the DVA. The red solid curve denotes the calibrated optimal status of the DVA with the minimum resonant response at point *P*. Even the fixed-points *P* and *Q*, at ω_{n1} and ω_{n2}, respectively, are not tightly coupled like in the traditional hanging DVA and ground-hooked DVA with local optimization. The response near the fixed-point *Q*, better observed in enlarged view, shows that the second peak is small and only clearly displayed with light damping. Therefore, the response near the fixed-point *P* is mainly concerned in the present analysis with varying damping. With the increasing damping ratio, the peak response amplitude decreases until reaching the fixed-point *P*, with damping ratio ξ being about 0.66 as shown in Fig. 4b, before increasing again when ξ exceeds 0.66. The corresponding frequency of the new peak locates at $\omega_n = \sqrt{(k_1 + k_2)/m_1}$, where the DVA system is deduced as a SDOF system with increased stiffness. Moreover, the optimal damping ratio in this case is about 0.66, which is much higher than that of the traditional hanging DVA. Since the proposed EMSD + VNIC + FD can provide a large tunable range of the damping force, it is suitable to be used for the experimental verification of the theoretical optimization of the ground hooked DVA derived by Cheung and Wong [63].

3. Damping enhancement

The mechanical structures of the prototypes, namely EMSD + FD and EMSD + VNIC, are presented and discussed in this section. The corresponding tuning methodology for each prototype is described in detail. Damping enhancement arising from each method is then quantified by hysteresis loop measurements and evaluated with either EMSD or FD as the damping tuning device. The measured spectrum of the damping force from FD is compared with the theoretical prediction in Section 2.2.2.

3.1 Structural parameters

As illustrated in Fig. 5, the tuning structures of the FD and EMSD are similar to that in ref. [43]. The normal force in the tunable FD in Fig. 5a can be tuned by changing the deformation of the tuning springs which is then kept constant due to the symmetrical compression springs. The total deformation of the tuning springs remains unchanged even with disturbance in the translational direction. The tunable damping amplitude of the FD can be expressed as

$$\left|F_f\right| = \mu_f k_f \Delta s = \mu_f k_f (s_0 - s) \tag{9}$$

where Δs denotes the deformation of the tuning springs, s the distance between the left and right nuts on the tuning screw, s_0 the initial distance when the friction blocks are just connected, k_f the stiffness of tuning spring. The product $\mu_f k_f$ can be regarded as one constant and obtained by measuring Δs in the translational direction and F_f in the vertical direction. $\mu_f k_f$ after linear fitting of the measured data is

shown in Table 1.

Table 1 Parameters of EMSD + FD and EMSD + VNIC

Enhancement method	Notation	Value or description
EMSD + FD	$\mu_f k_f$	125 N/m
	K_t	8.0242 N·s/m
	R_{in}	2.25 Ω
EMSD + VNIC	R_1	1 MΩ
	R_2	1 MΩ
	R_3	0-10 Ω
	OP-AMP	Apex PA75CD

The EMSD in Fig. 5b can be tuned by its adjusting the external resistance of its circuit as illustrated in Fig. 1a. The transduction factor K_t of the EMSD is determined as

$$K_t = -\oint_{loop} B_r(x,r)dl \tag{10}$$

where $B_r(x,r)$ is the radial magnetic flux density which varies with height and radius. dl is the unit arc length of a coil loop. The K_t calculated according to Eq. (10) is also shown in Table 1. The internal resistance R_{in} is measured using an ohmmeter. Moreover, since the inductive impedance of the coil is rather small in comparison to R_{in}, especially when EMSD is applied at low frequency, it is therefore not listed here.

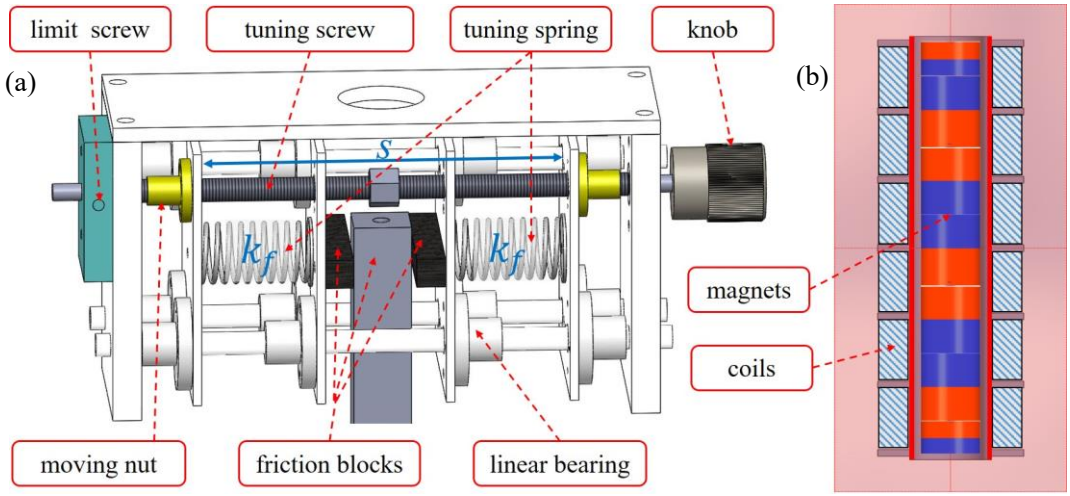

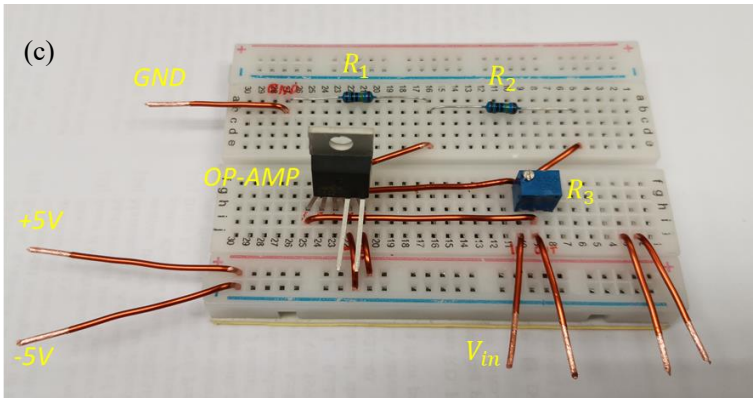

Fig. 5 3D models of (a) tunable FD and (b) EMSD, (c) the prototype of VNIC. For FD, the normal force and the subsequent resultant damping force on the friction blocks can be adjusted by rotating the knob to tuning the spring compression length. The damping force of the EMSD is tuned by changing the connected shunt resistance. For VNIC, four components are included: one OP-AMP for voltage amplification, one variable resistor R_3 of 0~10 Ω for the negative VNIC resistance adjustment, and two resistors R_1 and R_2 of 1 MΩ each.

The other enhancement method, EMSD + VNIC shunt is constructed as shown in Fig. 5c based on the schematics in Fig. 1b. Tunable resistance R_3 is used for equivalent negative resistance adjustment. Required connection terminals are labeled and the corresponding parameters of the components are listed in Table 1. It should be noted that the tunable range of R_3 should be limited so that the generated negative resistance would not be too close to R_{in}; otherwise, the excessive current may cause the overheating in the circuit.

3.2 Hysteresis Loops

To verify the efficacy of both enhancement methods, hysteresis loops with various combinations of FD and VNIC are measured with excitation at 10 Hz and vibration amplitude of 1 mm as shown in Fig. 6. A force sensor and a laser displacement sensor are used to measure the damping force and the displacement of the proposed damper simultaneously. The magnet bar of the EMSD and the friction block are connected with a coupling. Then the long bar connecting the magnets and the friction block is fixed on the floor with a strong magnet base. The displacement sensor is fixed on the support. Therefore, the damping force is measured at the fixed end while the displacement at the moving end of the dampers.

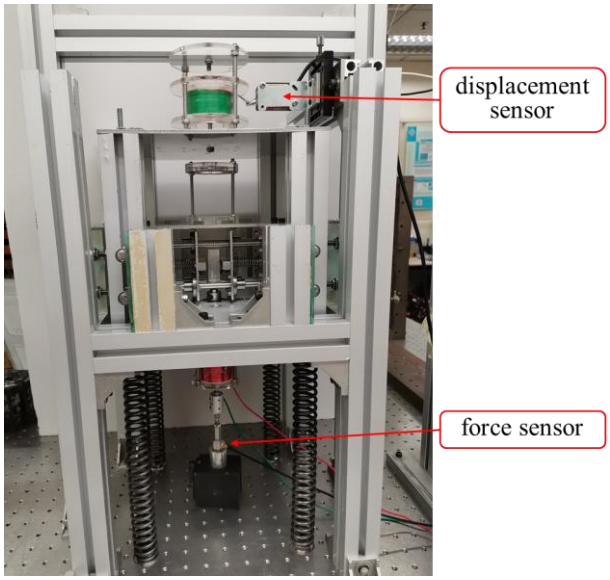

Fig. 6 Experimental setup for hysteresis loop measurement. The force sensor measures the damping force. The laser displacement sensor measures the displacement of the vibrating mass.

The measured hysteresis loops are plotted in Fig. 7. The hysteresis loops of the pure EMSD with different R_{load}, are shown in Fig. 7a. Those of the EMSD + VNIC with zero R_{load} and different values of negative resistance are shown in Fig. 7b. Comparing the hysteresis loops in Fig. 7b to Fig. 7a, Fig. 7b covers significantly larger areas than those in Fig. 7a, which means EMSD + VNIC can provide a higher tunable damping range than a pure EMSD. Due to the surface roughness, wear, thermal and lubricant state of the FD, the hysteresis loops with different tuning spring deformations become rough in the case of pure FD in Fig. 7c, EMSD+FD in Fig. 7d, and EMSD+VNIC+FD in Fig. 7e and Fig. 7f. However, with the increasing proportion of EMSD damping (increasing α) in Fig. 7d to Fig. 7f, hysteresis loops become much smoother than that with a pure FD as shown in Fig. 7c.

The positive slope observed for the case of EMSD only and EMSD with VNIC in Fig. 7a and Fig. 7b signifies an additional stiffness during the hysteresis loop measurement. The main reason is due to the large length-to-diameter ratio of the long bar connecting the magnets and the friction block in Fig. 6. The total length of the fixed bar is over 400 mm and the equivalent diameter is about 15 mm. The bar can possibly tilt when the mass of the DVA moves upward because of the large length to diameter ratio of the bar, thus generating additional stiffness in the system.

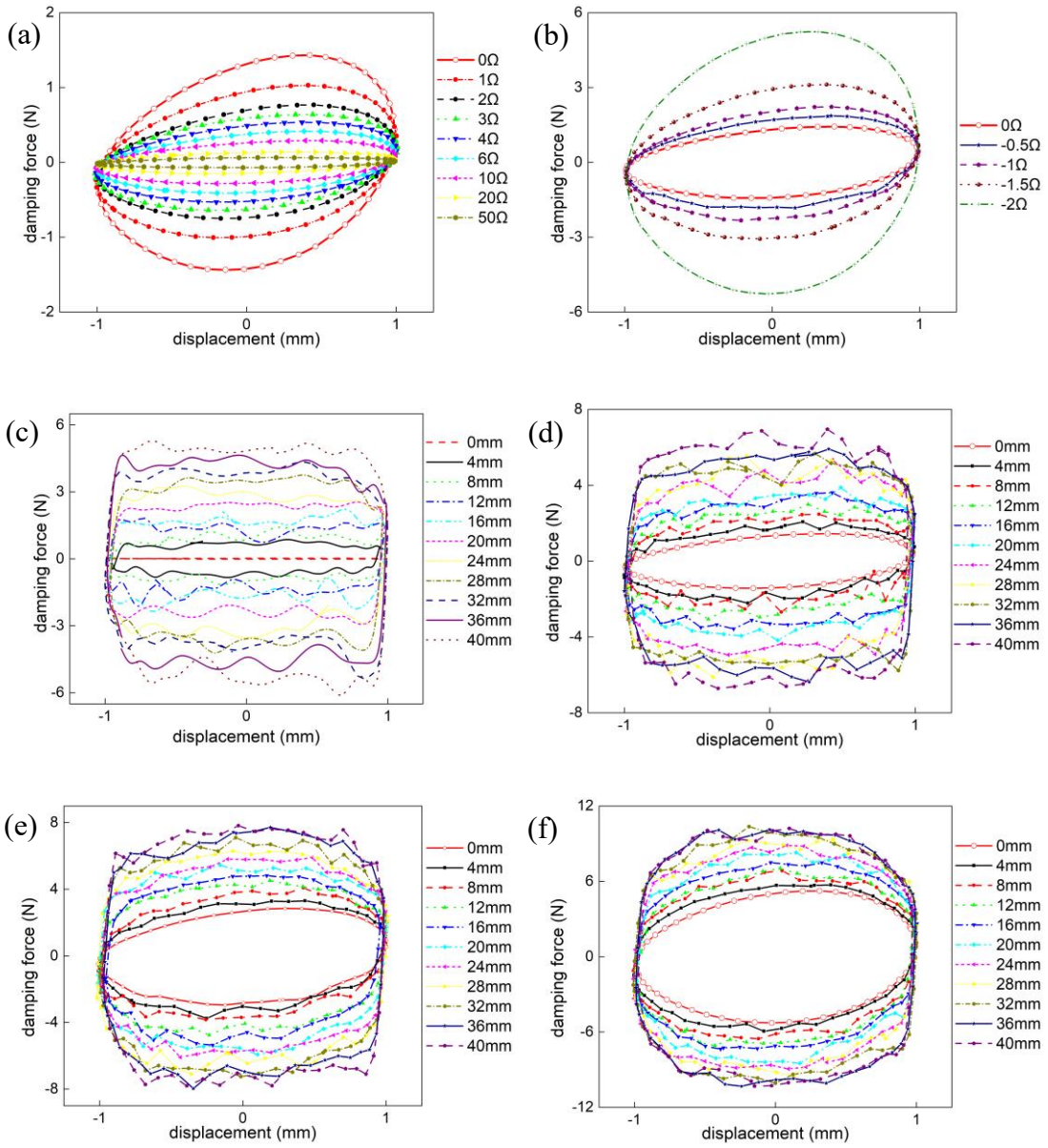

Fig. 7 Hysteresis loops of the dampers with different configurations when the excitation frequency is 10 Hz and the displacement amplitude is 1 mm. (a) EMSD with external shunt resistance from 0 Ω to 50Ω. (b) EMSD + VNIC (R_{VNIC}= 0 to -2 Ω). (c) FD, spring deformation from 0 mm to 40 mm. (d) EMSD + FD, spring deformation varies from 0 mm to 40 mm. (e) EMSD + VNIC (R_{VNIC}= -1 Ω) + FD, spring deformation from 0 mm to 40 mm. (f) EMSD + VNIC (R_{VNIC}= -2 Ω) + FD, spring deformation from 0 mm to 40 mm.

3.3 Enhancement analyses

The damping coefficients and the corresponding damping force in the proposed EMSD-based hybrid damper can be determined from the measured hysteresis loops with different configurations. Detailed damping enhancement results derived from measurements in Section 3.3.1 are compared with the theoretical predictions. The frequency spectra of the damping force in the hybrid damper are also measured in

Section 3.3.2 and compared with the theoretical results

3.3.1 Damping coefficient

The damping coefficients of the proposed dampers in the previous section are calculated using Eq. (11) below according to the corresponding hysteresis loops in Fig. 7.

$$c = \frac{\Delta U}{\pi \omega X} = \frac{U_1 - U_0}{2\pi^2 f X} \tag{11}$$

where ΔU is the energy loss, which can be evaluated by the enclosed area of the hysteretic loop. U_1 denotes the energy lost per cycle of the damper with a specific combination; U_0 the energy loss with system parasitic damping. The damping variation with EMSD shunt resistance or tuning spring deformation of FD are then plotted in Fig. 8 with EMSD or FD selected as the tuning device.

In Fig. 8a, black dots represent the measured damping coefficient of the EMSD, and blue dots represent EMSD+FD. The cyan region represents the case in which VNIC is connected to the EMSD shunt to provide negative resistance. Fig. 8a shows a similar trend as the theoretical prediction in Fig. 2a. The black dots with zero shunt resistance show the maximum damping provided by the pure EMSD, and the blue dots with a shunt resistance of -2 Ω represent the maximum damping of the EMSD + VNIC + FD. As shown in Fig. 8a, the rapid variation of the damping coefficient of EMSD + VNIC indicates that the tuning of damping in this area requires accurate resistance adjustment. The measured results show that the maximum damping coefficient of the EMSD can be increased from 21.3 N·s/m to 180.5 N·s/m when both EMSD+FD and VNIC are applied. The tunable range of the damping coefficient of the EMSD is increased from 1.0361 - 21.3251 N·s/m to 1.0361 - 180.5086 N·s/m by incorporating VNIC and FD to the EMSD as described before.

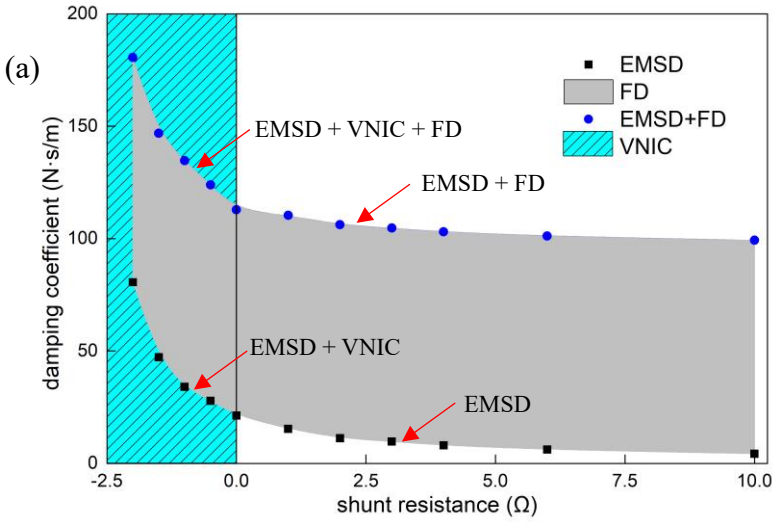

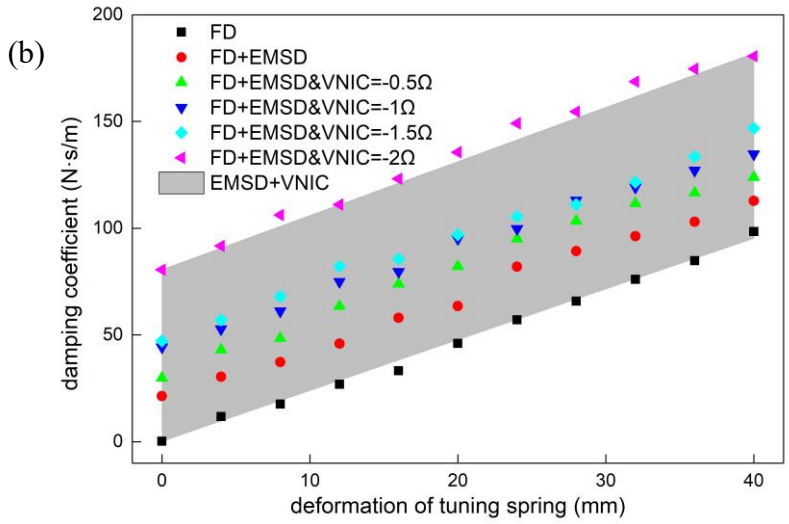

Fig. 8 Measured tunable damping coefficient of EMSD with different enhancement methods. (a) EMSD shunt resistance varies with fixed friction damping (inherent parasitic damping and friction damping with maximum normal force). (b) FD tuning spring deformation varies with fixed EMSD shunt resistance (R_{VNIC}=0 Ω, -0.5 Ω, -1 Ω, -1.5 Ω, -2 Ω).

Moreover, similar to the theoretical results in Fig. 2b, the measured damping coefficient in Fig. 8b increases linearly with the tuning spring deformation if FD is selected as the tuning device. The gray area denotes the damping contribution of the EMSD with VNIC. The linear damping variation with tuning spring deformation is more suitable for onsite tuning than that with VNIC as the tuning device. The detailed tunable ranges of the damping coefficient in different enhancement methods of EMSD are tabulated in Table 2. The maximum increase of the damping coefficient tunable range is about 900%.

Table 2 Tunable range with different types of dampers

Damper type	Tunable range (N·s/m)
EMSD	1.0361 - 21.3251
EMSD + VNIC (R_{VNIC}= -2 Ω)	1.0361 - 80.5973
FD	1.0361 - 92.4777
EMSD + FD	1.0361 - 112.8701
EMSD + FD + VNIC (R_{VNIC}= -0.5 Ω)	1.0361 - 123.9457
EMSD + FD + VNIC (R_{VNIC}= -1 Ω)	1.0361 - 134.7150
EMSD + FD + VNIC (R_{VNIC}= -1.5 Ω)	1.0361 - 146.8370
EMSD + FD + VNIC (R_{VNIC}= -2 Ω)	1.0361 - 180.5086

3.3.2 Hybrid damping force

Even the tunable damping range has been significantly enhanced, the multi-frequency response still requires experimental verification. To this end, the measured hybrid damping force with variable damping force ratio α and the corresponding simulation results based on Eqs. (4) and (5) are plotted in Fig. 9, showing rather consistent phenomena. Both the simulation and measurement results show that odd-order harmonics can be attenuated when α increases. Slight response at the frequency ratio 2 also occurs in measurements. This can be attributed to the slight offsetting of the center alignment when coupling the two components from EMSD and FD. In fact, the magnet bar of the EMSD and the friction block of FD are connected with a coupling as shown in Fig. 6. It is difficult for the axes of the two components to be aligned very precisely with manual adjustment. With the consideration of aforementioned tuning device selections, FD tuning with a fixed VNIC shunt seems to be a better choice to minimize multi-frequency response and satisfy the precise resistance tuning requirement of the VNIC.

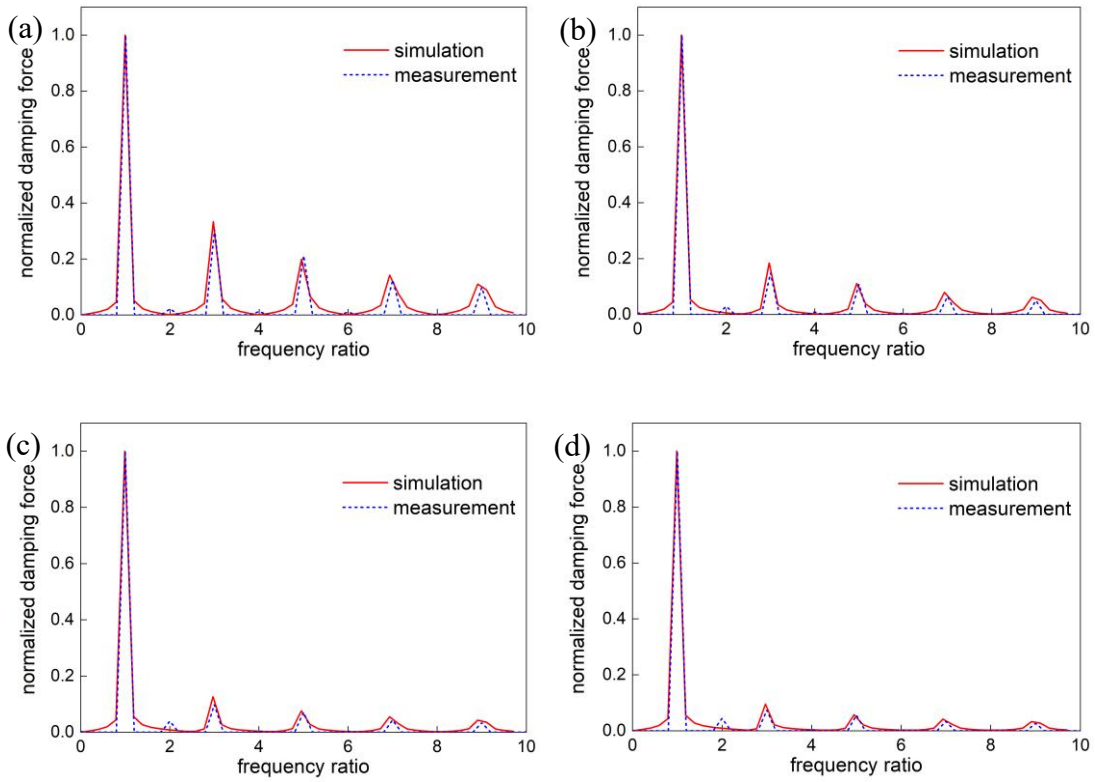

Fig. 9 The hybrid damping force spectra at different damping force ratios. (a) α=0, (b) α=1, (c) α=2, (d) α=3.

4. Hybrid damper applied to a ground-hooked DVA

In order to show the efficacy of the proposed EMSD based hybrid damper (EMSD+VNIC+FD) and the benefit arising from the expected large tunable damping

range, the proposed hybrid damper is experimentally tested. Meanwhile, experiments would allow verifying the theoretical optimal design proposed by Cheung and Wong [63] of the ground-hooked DVA. The experimental setup used for testing the proposed hybrid damper and the DVA is introduced in this section. The hybrid damper and the DVA are applied to a SDOF primary system for the minimization of the resonant vibration of the primary system. The DVA is optimized through proper tuning of the hybrid damper; and the primary system responses at various settings of the hybrid damper are measured and analyzed.

4.1 Experimental setup

As shown in Fig. 10, an experimental setup of a ground-hooked DVA is designed based on the theoretical model in Fig. 4a. The tuning mechanism of the FD and the coils of EMSD are fixed on the floor together. Since both the moving parts of the EMSD and the FD (magnet bar of the EMSD and the friction block of the FD) are coupled together, the two dampers are actually connected in parallel, like the one shown in Fig. 1a. The EMSD coil, external resistor, and VNIC shunt are connected in series as shown in Fig. 10. The added VNIC in Fig. 10d can reduce the total ESMD circuit impedance to almost zero. Four roller bearings on each side are used to provide a linear guide for the moving mass of the primary system. A force sensor and a laser displacement sensor are used to measure the exciting force and displacement signals of the primary system, respectively. An additional laser displacement is used to monitor the displacement of the auxiliary DVA, which is not shown in this photograph to avoid shadowing the main parts of the DVA system.

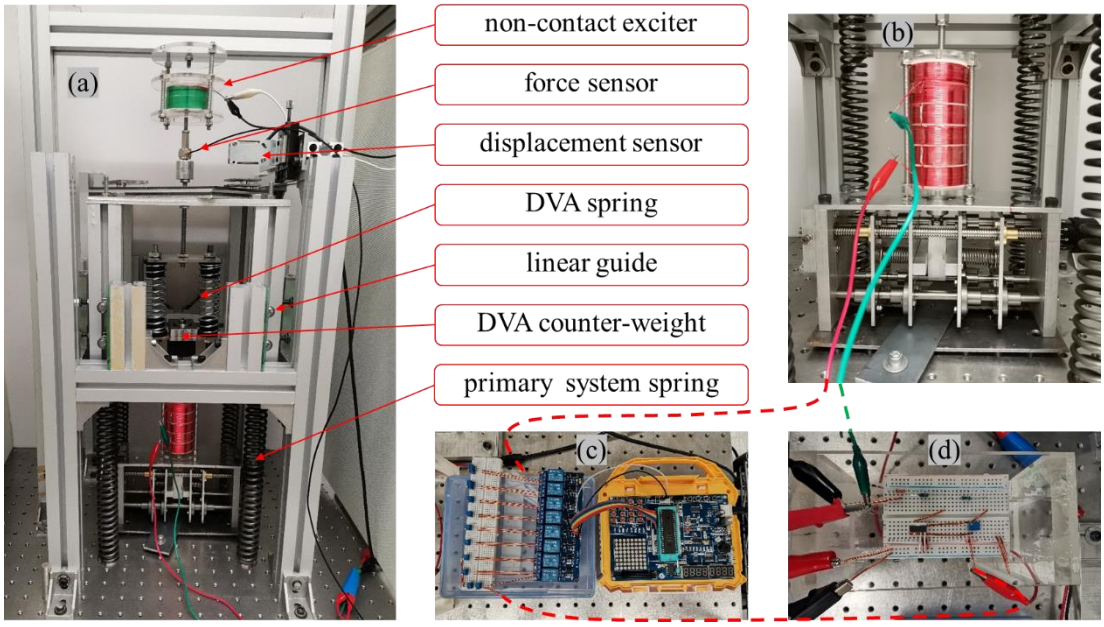

Fig. 10 Experimental setup. (a) Overall view. (b) EMSD+FD. (c) Variable resistor. (d) VNIC. The connection wires among the coil ends, external tunable resistor, and VNIC are shown as the dash lines in red between (b) and (c), (c) and (d), and in green between (b) and (d).

Data acquisition and signal generation are conducted with a B&K PULSE 7767

system. The driving signal to the exciter is amplified by a B&K 2712 power amplifier before being sent to the non-contact exciter. A B&K 8200 force sensor is used on the top to monitor the shaking force input from the non-contact exciter. With 1.5 Hz/s swept-sinusoidal excitations injected into the system via the exciter, the corresponding response can be recorded by two laser displacement sensors: one located on the top side support for measuring the displacement of primary mass, while the other measures the displacement response of the DVA mass (the corresponding figure is not given in Fig. 10a to avoid shielding other components). The natural frequency of the primary system is tuned to 9.5 Hz by changing the primary mass before the DVA is added to the system. As shown in Table 3, the optimal damping ratio ξ_{opti} of the ground-hooked DVA is much higher than that in traditional hanging DVAs. Other relative parameters are listed in Table 3.

Table 3 Parameters of ground-hooked DVA system

Notation	Value or description
k_1	20.961 N/mm
k_2	6.707 N/mm
m_1	5.8 kg
m_2	0.6 kg
μ	0.1035
ξ_{opti}	0.675

The large current induced in the circuit when the impedance is decreased near to zero affects the performance of the EMSD, particularly when the test is conducted continuously. Two methods are adopted in the experiments to reduce the influence of the generated heat: (1) intermittent tests to ensure that the testing devices are completely cooled down before another test is conducted; (2) usage of a cooling fan to cool down the EMSD and the shunt circuit.

4.2 Results analyses

In this section, a ground-hooked DVA with optimal damping is tested with the proposed hybrid damper involving different combinations of enhancement methods. The measurements of the primary system response with different enhancement configurations are conducted. Since the FD damping coefficient depends on the vibration amplitude and frequency, its real-time damping coefficient is also analyzed in this section for an in-depth study of the FD in the proposed hybrid damper.

4.2.1 Primary system response

With various combinations of EMSD enhancement methods, the spectra of displacement response of mass m_1 are measured and plotted in Fig. 11. The bold red solid curves in Fig. 11b to Fig. 11f denote optimally tuned response amplitude of m_1

with combination of EMSD, VNIC, and FD. EMSD alone cannot provide the optimal damping required for the ground-hooked DVA. EMSD with VNIC in Fig. 11b can reach the optimal damping, but the system may become unstable since the required circuit impedance is almost zero.

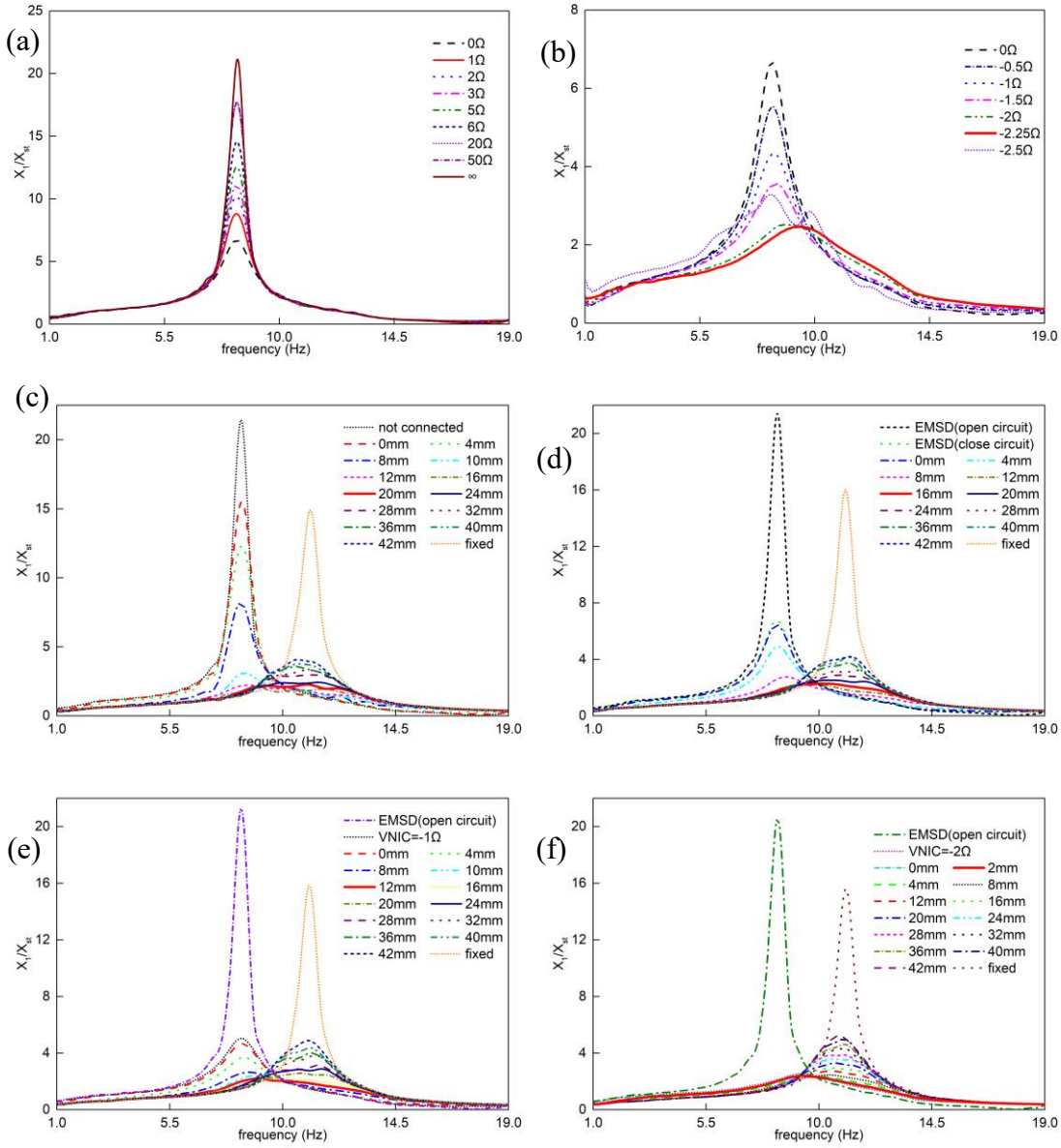

Fig. 11 Primary mass response of the ground-hooked DVA system with the various combined dampers. (a) EMSD with external shunt resistance from 0 Ω to infinity. (b) EMSD + VNIC (R_{VNIC}= 0 to -2 Ω). (c) FD with spring deformation from 0 mm to 40 mm. (d) EMSD + FD with spring deformation from 0 mm to 40 mm. (e) EMSD + VNIC (R_{VNIC}= -1 Ω) + FD with spring deformation from 0 mm to 40 mm. (f) EMSD + VNIC (R_{VNIC}= -2 Ω) + FD with spring deformation from 0 mm to 40 mm.

A new peak of deduced SDOF system will appear when the damping continues to increase after reaching the optimal damping as mentioned in Section 2.3. New peaks located at around 11.5 Hz in Fig. 11c to Fig. 11f demonstrate that damping is highly

improved after adding the FD. The optimal damping can be achieved with FD alone when the tuning spring deformation is around 20 mm. If both VNIC and FD are added to the EMSD with VNIC being tuned first, the required tuning spring deformation of the FD decreases from 16 mm to 2 mm. As discussed in Section 3.3.2, the response curve of the primary mass in Fig. 11f becomes much smoother with the additional damping provided by the VNIC-based EMSD than the FD. Displacement response with different damping ratios does not pass the fixed point exactly, particularly when the damping provision is mainly from the FD. Two factors contribute to this observed deviation from the fixed point: the damping fluctuation due to the uneven roughness of the contacting plate and possible partial stick-slip when the normal force is large. For the former, the measured hysteresis loops in Fig. 11c to Fig. 11f show that the damping coefficient curve is not as smooth as the one from the EMSD. For the second factor, the stick-slip phenomenon occurs when the friction force is larger than $\pi/4$ of the exciting force as shown by the equation below.

$$\frac{\mu_f F_N}{F_0} > \frac{\pi}{4} \tag{12}$$

4.2.2 Optimal DVA

Fig. 11b to Fig. 11f show five different combinations of EMSD, VNIC, and FD to provide the optimal damping of the ground-hooked DVA system. The corresponding parameters of the five optimal damping combinations are listed in Table 4. The damping coefficient of the EMSD+VNIC can be increased by increasing the negative resistance provided by the VINC, but the EMSD circuit resistance becomes close to zero, leading to overcurrent in the circuit. Moreover, the optimized primary mass response curves are plotted in Fig. 12 with both theoretical results and calibrated experimental results under five combinations.

Table 4 Five types of optimal damping combinations

Combinations	Tuning spring deformation of FD (mm)	Circuit resistance of EMSD (Ω)	α at 10 Hz
FD	20	N/A	0
EMSD+FD	16	2.25	1
EMSD+FD+VNIC (R_{VNIC}= -1 Ω)	12	1.25	1.67
EMSD+FD+VNIC (R_{VNIC}= -2 Ω)	2	0.25	12.5
EMSD+VNIC (R_{VNIC}= -2.25 Ω)	N/A	0	N/A

The optimal response curve in Fig. 12 with EMSD+VNIC is the closest one to the theoretical results [63] and it is smoother than the other curves with FD. Friction damping provided by the FD may be affected by the surface roughness, wear, thermal and lubricant states of the friction blocks of the FD. Therefore, some ripples appear on the response curve corresponding to FD. Therefore, the damping provided by the FD is not as smooth as the one by EMSD with VNIC. In the present case, EMSD with VINC can already ensure the optimal status of the ground-hooked DVA without using FD. For more general cases, a better choice is to select the suitable VNIC with stability for the basis then tune the FD in a smaller range for optimal damping calibration.

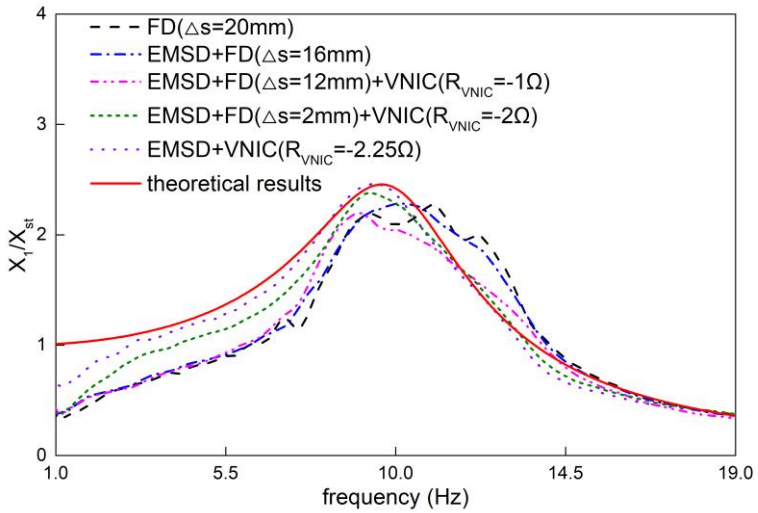

Fig. 12 Comparison between theoretical and experimental results of H_∞ optimized primary system responses. Five calibrated damping configurations are included, (1) black dash line: FD only with 20 mm spring deformation; (2) blue dash dot line: EMSD + FD with 16 mm spring deformation; (3) magenta dash dot line: EMSD + VNIC (R_{VNIC}= -1 Ω) + FD with 12 mm spring deformation; (4) short dash line: EMSD + VNIC (R_{VNIC}= -2 Ω) + FD with 2 mm spring deformation; (5) purple dot line: EMSD + VNIC (R_{VNIC}= -2.25 Ω).

4.2.3 Real-time damping

Onsite damping tuning of the EMSD with FD or VNIC is proved effective for ground-hooked DVA implementation with experimental results in the previous section. In this section, the primary mass is excited as described in Section 4.1 with a sweep frequency rate of 1.5 Hz/s and the time-displacement curves of DVA mass with FD are measured and plotted as blue solid lines in Fig. 13a to Fig. 13d. The equivalent damping coefficient of the FD changes with frequency, and also with the time when the displacement amplitude changes according to Eq. (1). The corresponding displacement amplitude can be extracted and plotted as the red dot lines through extracting the upper envelope of the response signals. The exact frequency with time can be identified with the start time for each and the sweep rate of 1.5 Hz/s. Then, the real-time equivalent damping coefficient can be obtained and plotted as Fig. 13e based on Eq. (1) for further analyses of different damper designs.

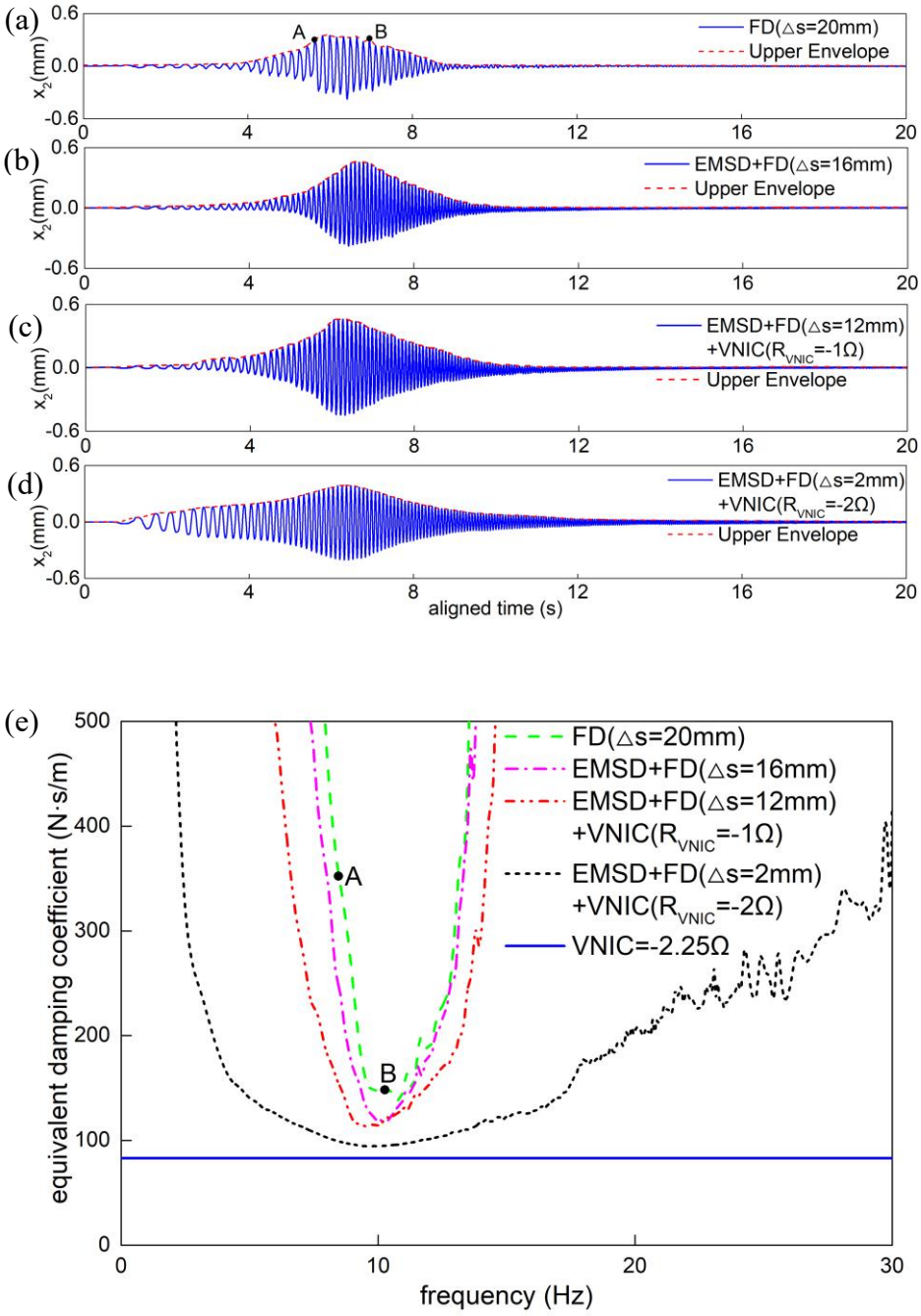

Fig. 13 Displacement response of DVA mass with four types of damping combinations. (a) FD only with 20 mm spring deformation. (b) EMSD + FD with 16 mm spring deformation. (c) EMSD + VNIC (R_{VNIC}= -1 Ω) + FD with 12 mm spring deformation. (d) EMSD + VNIC (R_{VNIC}= -2 Ω) + FD with 2 mm spring deformation. (e) Equivalent damping coefficient of five types of damper configuration based on Eq. (1). *A* and *B* in subfigures (a) and (e) are two selected points with the same displacement amplitude to verify the frequency influence on the equivalent damping coefficient.

The same force amplitude is applied by the non-contact exciter during the frequency sweep test. The response of m_1 in the tested system with FD (Fig. 13a) shows

a maximum response at about 10 Hz. According to Eq. (1), the damping coefficient of FD is inversely proportional to the product of the frequency and the vibration amplitude. Therefore, the minimum damping coefficient observed on the FD curve in Fig. 13e of the revised manuscript also appears at about 10 Hz. As to the frequency effect on the damping coefficient of the FD alone, the two points *A* and *B*, having the same vibration amplitude in Fig. 13a, are considered. Both *A* and *B* correspond to a vibration amplitude of 0.3 mm. Point A appears at 5.6266 s with 8.44 Hz, and B appears at 6.7333 s with 10.10 Hz. The damping coefficients at A and B can be determined to be 354 N·s/m and 152 N·s/m based on the FD damping part of Eq. (1). The results show that the damping coefficient at 8.44 Hz is much larger than that at 10.10 Hz. With the same vibration amplitude, a lower frequency leads to a higher damping coefficient.

The damping coefficient of a linear EMSD (about 85 N·s/m with R_{VNIC}=-2.25 Ω) is taken in Fig. 13e as the benchmark for comparison with other damper configurations. The curves from FD to EMSD+VNIC in Fig. 13e correspond to increasing values of α from zero to the maximum as arranged from top to the bottom in the legend. The main findings from the analysis of Fig. 13e are listed below:

1. All four damping coefficient curves with FD are above the reference line of 85 N·s/m (EMSD+VNIC). The damping force of the FD contains multi-frequency components as illustrated in Fig. 9. The required equivalent damping (85 N·s/m) on target frequency (around 10 Hz) from FD will bring the accompanying multi-frequency components, which results in the over-estimated damping coefficient at the target frequency.

2. With increasing α, the damping coefficient of the dampers with FD approaches 85 N·s/m (EMSD+VNIC with R_{VNIC}= -2.25 Ω). A higher α corresponds to a higher damping force provided by EMSD than FD, and the effect of the aforementioned multi-frequency components of FD is reduced.

3. The FD curve in Fig. 13e shows a very narrow insensitive frequency range of the equivalent damping coefficient. The very high frequency sensitivity of the FD limits the hybrid damping stability. The hybrid damping with a higher FD contribution (small α) becomes more sensitive to frequency because the equivalent damping of the FD depends on both vibration frequency and vibration amplitude. As shown by other curves in Fig. 13e, an increase in the damping in the hybrid EMSD damper can widen the insensitive frequency range of the FD. This observation from Fig. 13e is consistent with the hybrid damping force analyses in Section 3.

4.3 Unstable VNIC

When the total impedance of the EMSD circuit is reduced to almost zero after adding the VNIC, the electric circuit becomes less effective in dissipating energy, which is equivalent to a reduction of the damping coefficient. The reason is due to the voltage saturation of the VNIC, which has been stated in detail by Li [13]. Moreover, when the total circuit impedance is negative, EMSD will introduce negative damping to the system which will make the whole system unstable [11].

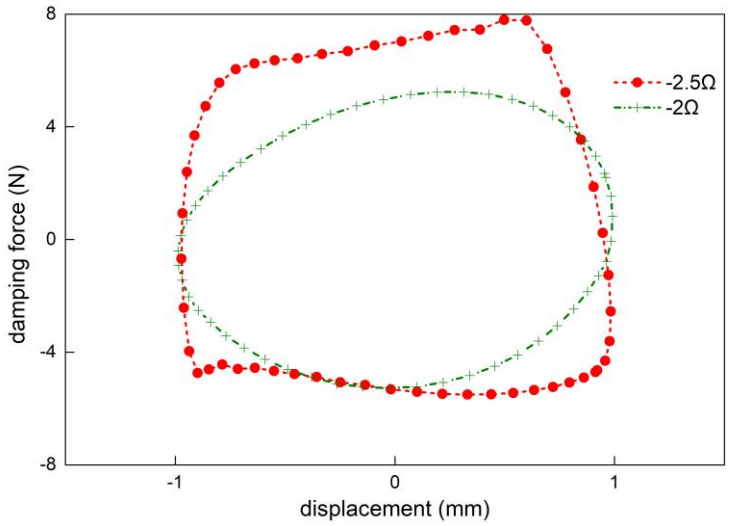

Fig. 14 Hysteresis loops of EMSD+VNIC when the total circuit impedance is near zero with dot symbols (R_{VNIC}= -2 Ω) and less than zero with plus symbols (R_{VNIC}= -2.5 Ω).

The above investigations show that higher linear damping of the EMSD with VNIC contributes to the damping stability. Therefore, the higher linear damping from EMSD, the better, as long as the EMSD circuit remains stable. Since the internal resistance of the EMSD is about 2.25 Ω, the equivalent resistance of the VNIC should not be smaller than -2.25 Ω. The hysteresis loops of EMSD with R_{VNIC}=-2 Ω and R_{VNIC}=-2.5 Ω are measured and plotted in Fig. 14 for understanding the effect of the VNIC on the linearity of damping force of EMSD+VNIC. The total circuit impedance of EMSD is near zero when R_{VNIC}=-2 Ω. The corresponding hysteresis loop still appears as an ellipse of a linear damper as shown in Fig. 14. However, the hysteresis loop is distorted, as shown by the red dotted curve in Fig. 14, when the total circuit impedance is less than zero with R_{VNIC}=-2.5 Ω. Moreover, fluctuations in the primary system response with R_{VNIC}=-2.5 Ω in Fig. 11b also evidence the instability of the EMSD damping.

5. Conclusions

Two enhancement methods, namely EMSD with VNIC and EMSD with FD, are analyzed, both numerically and experimentally, for increasing the damping force-to-mass ratio and the tunable damping range of EMSD. EMSDs with VNIC, FD, or their combination are designed and tested experimentally for damping enhancement. The tunable range of the damping coefficient of the proposed EMSD is shown to be increased by about 900% after adding both VNIC and FD (EMSD+VNIC+FD) by following the proposed design procedure.

The damping force of the proposed hybrid damper is evaluated to maximize the respective advantages of the individual component of the hybrid damper. With the increase of the linear damping from EMSD (high damping ratio α), the nonlinear effect of the damping force of the FD can be significantly attenuated in the proposed hybrid damper. The proposed design procedure leads to an enhanced EMSD, in which the FD and VNIC are tactically added to supplement each other to increase the damping range

of the EMSD on one hand, and to avoid the possible instability of the EMSD due to the use of VNIC and the high frequency sensitivity of the FD on the other hand. The damping force-to-mass ratio of the proposed hybrid damper (EMSD+VNIC+FD) is shown to be increased by about 600% from the original EMSD.

To show the effectiveness of the proposed hybrid damper for vibration control applications which require precise damping tunability and a relatively high damping force-to-mass ratio, the proposed hybrid damper is applied to a ground-hooked DVA and tested experimentally. Results confirm that the H_∞ optimization of the ground-hooked DVA can be readily achieved for the minimization of resonant vibration of a single DOF dynamic system.

Acknowledgments

The authors would like to acknowledge the Research Grant Council of Hong Kong for the funding support (Project number: 15206120).

Appendix A. Equivalent resistance of VNIC

Since no current flows between V_+ and V_-, the amplified output voltage can be expressed as

$$V_{out} = \frac{V_-}{R_1}(R_1 + R_2) \tag{A1}$$

where R_1 and R_2 are the two selected constant resistance for the VNIC.

The current flow through R_3 can be calculated as

$$R_3 = \frac{V_+ - V_{out}}{i} \tag{A2}$$

where R_3 is a variable resistance of the VNIC. Assuming $V_+ = V_-$, the VNIC equivalent resistance can be expressed as

$$R_{VNIC} = \frac{V_{in}}{i} = -\frac{R_1 R_3}{R_2} \tag{A3}$$

Appendix B. Motion equations of DVA

The motion equations of the primary mass m_1 and DVA mass m_2 write

$$m_1\ddot{x}_1 + k_1 x_1 + k_2(x_1 - x_2) = F_0 \cos \omega t \tag{B1}$$

$$m_2\ddot{x}_2 + k_2(x_2 - x_1) + c_2\dot{x}_2 = 0 \tag{B2}$$

By solving the differential equations, the dimensionless displacement response amplitude of the primary mass m_1, X_1/X_{st}, can then be expressed as

$$\left|\frac{X_1}{X_{st}}\right| = \sqrt{\frac{(2\xi\lambda)^2 + (\lambda^2 - \gamma^2)^2}{(2\xi\lambda)^2(1 + \mu\gamma^2 - \lambda^2)^2 + [\mu\gamma^2\lambda^2 - (\lambda^2 - 1)(\lambda^2 - \gamma^2)]^2}} \quad \text{(B3)}$$

References

[1] Pan Y, Liu F, Jiang R, Tu Z, Zuo L. Modeling and onboard test of an electromagnetic energy harvester for railway cars. Appl Energ 2019;250:568-581. https://doi.org/10.1016/j.apenergy.2019.04.182

[2] Lafarge B, Grondel S, Delebarre C, Curea O, Richard C. Linear electromagnetic energy harvester system embedded on a vehicle suspension: From modeling to performance analysis. Energy 2021;225:119991. https://doi.org/10.1016/j.energy.2021.119991

[3] Yuan M, Liu K, Sadhu A. Simultaneous vibration suppression and energy harvesting with a non-traditional vibration absorber. J Intel Mat Syst Str 2018;29:1748-1763. https://doi.org/10.1177%2F1045389X17754263

[4] Zuo L, Cui W. Dual-functional energy-harvesting and vibration control: electromagnetic resonant shunt series tuned mass dampers. J Vib Acoust 2013;135: 051018. https://doi.org/10.1115/1.4024095

[5] Zhu S, Shen WA, Xu YL. Linear electromagnetic devices for vibration damping and energy harvesting: Modeling and testing. Eng Struct 2012;34:198-212. https://doi.org/10.1016/j.engstruct.2011.09.024

[6] Xie L, Li J, Li X, Huang L, Cai S. Damping-tunable energy-harvesting vehicle damper with multiple controlled generators: design, modeling and experiments. Mech Syst Signal Pr 2018;99:859-872. https://doi.org/10.1016/j.ymssp.2017.07.005

[7] Shen W, Zhu S, Zhu H. Experimental study on using electromagnetic devices on bridge stay cables for simultaneous energy harvesting and vibration damping. Smart Mat Struct 2016;25:065011. https://doi.org/10.1088/0964-1726/25/6/065011

[8] Yan B, Wang K, Kang CX, Zhang XN, Wu CY. Self-sensing electromagnetic transducer for vibration control of space antenna reflector. IEEE-ASME T Mech 2017;22:1944-1951. https://doi.org/10.1109/TMECH.2017.2712718

[9] Sun R, Wong W. Vibration control with a tunable self-sensing electromagnetic shunt damper. 23rd International Conference on Mechatronics Technology (ICMT) 2019:1-6. https://doi.org/10.1109/ICMECT.2019.8932148

[10] Behrens S, Fleming AJ, Moheimani SR. Electromagnetic shunt damping. In Proceedings 2003 IEEE/ASME International Conference on Advanced Intelligent Mechatronics (AIM 2003) 2003;2:1145-1150. https://doi.org/10.1109/AIM.2003.1225504

[11] Yan B, Zhang X, Luo Y, Zhang Z, Xie S, Zhang Y. Negative impedance shunted electromagnetic absorber for broadband absorbing: experimental investigation. Smart Mater Struct 2014;23(12):125044. https://doi.org/10.1088/0964-1726/23/12/125044

[12] Stabile A, Aglietti GS, Richardson G, Smet G. Design and verification of a negative resistance electromagnetic shunt damper for spacecraft micro-vibration. J Sound Vib 2017;386:38-49. https://doi.org/10.1016/j.jsv.2016.09.024

[13] Li JY, Zhu S. Versatile behaviors of electromagnetic shunt damper with a negative impedance converter. IEEE-ASME T Mech 2018;23:1415-1424. https://doi.org/10.1109/TMECH.2018.2813307

[14] Zhou S, Jean-Mistral C, Chesné S. Electromagnetic shunt damping with negative impedances: optimization and analysis. J Sound Vib 2019;445:188-203. https://doi.org/10.1016/j.jsv.2019.01.014

[15] Kamali SH, Miri MH, Moallem M, Arzanpour S. Cylindrical cam electromagnetic vibration damper utilizing negative shunt resistance. IEEE-ASME T Mech 2019;25:996-1004. https://doi.org/10.1109/TMECH.2019.2959523

[16] Berardengo M, Thomas O, Giraud-Audine C, Manzoni S. Improved shunt damping with two negative capacitances: an efficient alternative to resonant shunt. J Intel Mat Syst Str 2017;28:2222-2238. https://doi.org/10.1177%2F1045389X16667556

[17] Behrens S, Fleming AJ, Moheimani SR. Passive vibration control via electromagnetic shunt damping. IEEE-ASME T Mech 2005;10(1):118-122. https://doi.org/10.1109/TMECH.2004.835341

[18] Li JY, Zhu S. Advanced vibration isolation technique using versatile electromagnetic shunt damper with tunable behavior. Eng Struct 2021;242:112503. https://doi.org/10.1016/j.engstruct.2021.112503

[19] Auleley M, Giraud-Audine C, Mahé H, Thomas O. Tunable electromagnetic resonant shunt using pulse-width modulation. J Sound Vib 2021;500:116018. https://doi.org/10.1016/j.jsv.2021.116018

[20] Li JY, Zhu S. Tunable electromagnetic damper with synthetic impedance and self-powered functions. Mech Syst Signal Pr 2021;159:107822. https://doi.org/10.1016/j.ymssp.2021.107822

[21] Niederberger D, Behrens S, Fleming AJ, Moheimani SR, Morari M. Adaptive electromagnetic shunt damping. IEEE-ASME T Mech 2006;11:103-108. https://doi.org/10.1109/TMECH.2005.859844

[22] McDaid AJ, Mace BR. A self-tuning electromagnetic vibration absorber with adaptive shunt electronics. Smart Mater Struct 2013;22(10):105013. https://doi.org/10.1088/0964-1726/22/10/105013

[23] Jamshidi M, Chang CC, Bakhshi A. Design and control of a self-powered hybrid electromagnetic damper. J Sound Vib 2018;428:147-167. https://doi.org/10.1016/j.jsv.2018.05.004

[24] Paknejad A, Zhao G, Chesné S, Deraemaeker A, Collette C. Hybrid

electromagnetic shunt damper for vibration control. J Vib Acoust 2021;143:021010. https://doi.org/10.1115/1.4048389

[25] Yan B, Wang K, Hu Z, Wu C, Zhang X. Shunt damping vibration control technology: A review. Appl Sci 2017;7:494. https://doi.org/10.3390/app7050494

[26] Kremer D, Liu K. A nonlinear energy sink with an energy harvester: transient responses. J Sound Vib 2014;333:4859-4880. https://doi.org/10.1016/j.jsv.2014.05.010

[27] Sun R, Wong W, Cheng L. Tunable electromagnetic shunt damper with opposing magnets configuration. Smart Mater Struct 2020; 29: 115034. https://doi.org/10.1088/1361-665X/abb21d .

[28] Zuo L, Scully B, Shestani J, Zhou Y. Design and characterization of an electromagnetic energy harvester for vehicle suspensions. Smart Mater Struct 2010;19:045003. https://doi.org/10.1088/0964-1726/19/4/045003

[29] Sun R, Wong W, Cheng L. Optimal design of a tunable electromagnetic shunt damper for dynamic vibration absorber. Mechatronics 2022;83:102763. https://doi.org/10.1016/j.mechatronics.2022.102763

[30] Yan B, Wang X, Wang Z, Wu C, Zhang W. Enhanced lever-type vibration isolator via electromagnetic shunt damping. Int J Mech Sci 2022;218:107070. https://doi.org/10.1016/j.ijmecsci.2022.107070

[31] Li JY, Zhu S, Shen J. Enhance the damping density of eddy current and electromagnetic dampers. Smart Struct Syst 2019;24:15-26. https://doi.org/10.12989/sss.2019.24.1.015

[32] Ma H, Yan B, Zhang L, Zheng W, Wang P, Wu C. On the design of nonlinear damping with electromagnetic shunt damping. Int J Mech Sci 2020;175:105513. https://doi.org/10.1016/j.ijmecsci.2020.105513

[33] Yan B, Ma H, Zhao C, Wu C, Wang K, Wang P. A vari-stiffness nonlinear isolator with magnetic effects: Theoretical modeling and experimental verification. Int J Mech Sci 2018;148:745-755. https://doi.org/10.1016/j.ijmecsci.2018.09.031

[34] Yan B, Yu N, Ma H, Wu C. A theory for bistable vibration isolators. Mech Syst Signal Pr 2022;167:108507. https://doi.org/10.1016/j.ymssp.2021.108507

[35] Li JY, Zhu S, Shi X, Shen W. Electromagnetic shunt damper for bridge cable vibration mitigation: full-scale experimental study. J Struct Eng 2020;146(1):04019175. https://doi.org/10.1061/(ASCE)ST.1943-541X.0002477

[36] Cai QL, Zhu S. Enhancing the performance of electromagnetic damper cum energy harvester using microcontroller: Concept and experiment validation. Mech Syst Signal Pr 2019;134:106339. https://doi.org/10.1016/j.ymssp.2019.106339

[37] Lin T, Wang JJ, Zuo L. Efficient electromagnetic energy harvester for railroad transportation. Mechatronics 2018;53:277-286. https://doi.org/10.1016/j.mechatronics.2018.06.019

[38] Asadi E, Ribeiro R, Khamesee MB, Khajepour A. Analysis, prototyping, and experimental characterization of an adaptive hybrid electromagnetic damper for

automotive suspension systems. IEEE T Veh Technol 2016;66:3703-3713. https://doi.org/10.1109/TVT.2016.2606607

[39] Xia X, Zheng M, Liu P, Zhang N, Ning D, Du H. Friction observer-based hybrid controller for a seat suspension with semi-active electromagnetic damper. Mechatronics 2021;76:102568. https://doi.org/10.1016/j.mechatronics.2021.102568

[40] Ao WK, Reynolds P. Evaluation of optimal analysis, design, and testing of electromagnetic shunt damper for vibration control of a civil structure. Struct Control Hlth 2020;27:e2495. https://doi.org/10.1002/stc.2495

[41] Liu H, Gudla S, Hassani FA, Heng CH, Lian Y, Lee C. Investigation of the nonlinear electromagnetic energy harvesters from hand shaking. IEEE Sens J 2014;15:2356-2364. https://doi.org/10.1109/JSEN.2014.2375354

[42] Fan K, Cai M, Liu H, Zhang Y. Capturing energy from ultra-low frequency vibrations and human motion through a monostable electromagnetic energy harvester. Energy 2019;169:356-368. https://doi.org/10.1016/j.energy.2018.12.053

[43] Sun R, Wong W, Cheng L. A tunable hybrid damper with Coulomb friction and electromagnetic shunt damping. J Sound Vib 2022 ;524:116778. https://doi.org/10.1016/j.jsv.2022.116778

[44] Den Hartog JP. LXXIII. Forced vibrations with combined viscous and coulomb damping. The London, Edinburgh, and Dublin Philosophical Magazine and Journal of Science 1930;9:801-817. https://doi.org/10.1080/14786443008565051

[45] Menq CH, Griffin J H, Bielak J. The influence of a variable normal load on the forced vibration of a frictionally damped structure. J Eng Gas Turb Power 1986;108:300-305. https://doi.org/10.1115/1.3239903

[46] Lee JH, Berger E, Kim JH. Feasibility study of a tunable friction damper. J Sound Vib 2005;283:707-722. https://doi.org/10.1016/j.jsv.2004.05.022

[47] Dai W, Yang J, Wiercigroch M. Vibration energy flow transmission in systems with Coulomb friction. Int J Mech Sci 2022;214:106932. https://doi.org/10.1016/j.ijmecsci.2021.106932

[48] Marino L, Cicirello A, Hills DA. Displacement transmissibility of a Coulomb friction oscillator subject to joined base-wall motion. Nonlinear Dyn 2019; 98:2595-2612. https://doi.org/10.1007/s11071-019-04983-x

[49] Marino L, Cicirello A. Multi-degree-of-freedom systems with a Coulomb friction contact: analytical boundaries of motion regimes. Nonlinear Dyn 2021;104:35-63. https://doi.org/10.1007/s11071-021-06278-6

[50] Scholl M, Tiesler B, Müller G. Statistical evaluation of experimental and numerical data of stick–slip effects in harmonically excited systems. J Sound Vib 2022;517:116536. https://doi.org/10.1016/j.jsv.2021.116536

[51] Chen W, Deng X. Structural damping caused by micro-slip along frictional interfaces. Int J Mech Sci 2005;47:1191-1211. https://doi.org/10.1016/j.ijmecsci.2005.04.005

[52] Zhou R, Gu Y, Ren G, Yu S. Modelling and stability characteristics of bump-type gas foil bearing rotor systems considering stick–slip friction. Int J Mech Sci 2022;219:107091. https://doi.org/10.1016/j.ijmecsci.2022.107091

[53] Von Osmanski S, Larsen JS, Santos IF. A fully coupled air foil bearing model considering friction-Theory & experiment. Journal of Sound and Vibration. 2017;400:660-79. https://doi.org/10.1016/j.jsv.2017.04.008

[54] Ferri AA. Friction damping and isolation systems. J Vib Acoust 1995; 117: 196-206. https://doi.org/10.1115/1.2838663

[55] Gagnon L, Morandini M, Ghiringhelli GL. A review of friction damping modeling and testing. Arch Appl Mech 2020;90(1):107-126. https://doi.org/10.1007/s00419-019-01600-6

[56] Ruderman M, Iwasaki M. Observer of nonlinear friction dynamics for motion control. IEEE T Ind Electron 2015;62:5941-5949. https://doi.org/10.1109/TIE.2015.2435002

[57] Huang S, Liang W, Tan KK. Intelligent friction compensation: A review. IEEE-ASME T Mech 2019;24:1763-1774. https://doi.org/10.1109/TMECH.2019.2916665

[58] Weber F, Høgsberg J, Krenk S. Optimal tuning of amplitude proportional Coulomb friction damper for maximum cable damping. J Struct Eng 2010; 136(2):123-34. https://doi.org/10.1061/(ASCE)0733-9445(2010)136:2(123)

[59] Sinha A, Trikutam KT. Optimal vibration absorber with a friction damper. J Vib Acoust 2018;140:021015. https://doi.org/10.1115/1.4038272

[60] Den Hartog JP, Mechanical vibrations, Courier Corporation; 1985.

[61] Ren MZ. A variant design of the dynamic vibration absorber. J Sound Vib 2001;245:762-770. https://doi.org/10.1006/jsvi.2001.3564

[62] Liu K, Liu J. The damped dynamic vibration absorbers: revisited and new result. J Sound Vib 2005;284:1181-1189. https://doi.org/10.1016/j.jsv.2004.08.002

[63] Cheung YL, Wong WO. H-infinity optimization of a variant design of the dynamic vibration absorber—revisited and new results. J Sound Vib 2011;330:3901-3912. https://doi.org/10.1016/j.jsv.2011.03.027

[64] Zhu S, Shen W, Qian X. Dynamic analogy between an electromagnetic shunt damper and a tuned mass damper. Smart Mater Struct 2013;22:115018. https://doi.org/10.1088/0964-1726/22/11/115018

[65] Auleley M, Thomas O, Giraud-Audine C, Mahé H. Enhancement of a dynamic vibration absorber by means of an electromagnetic shunt. J Intel Mat Syst Str 2021;32:331-354. https://doi.org/10.1177/1045389X20957097

[66] Ikegame T, Takagi K, Inoue T. Exact solutions to H_∞ and H_2 optimizations of passive resonant shunt circuit for electromagnetic or piezoelectric shunt damper. J Vib Acoust 2019;141: 031015. https://doi.org/10.1115/1.4042819

[67] Ao WK, Reynolds P. Analysis and numerical evaluation of H_∞ and H_2 optimal design schemes for an electromagnetic shunt damper. J Vib Acoust 2020;142(2): 021003. https://doi.org/10.1115/1.4045455